Optics Letters

Enhancement in electro-optic performance of InAlGaAs/GaAs quantum dot lasers by *ex situ* thermal annealing

Weicheng You,[1,†] Riazul Arefin,[1,†] Fatih Uzgur,[1] Seunghyun Lee,[1] Sadhvikas J. Addamane,[2] Baolai Liang,[3] and Shamsul Arafin[1,*]

[1]*Department of Electrical and Computer Engineering, The Ohio State University, Columbus, Ohio 43210, USA*
[2]*Center for Integrated Nanotechnologies, Sandia National Laboratories, Albuquerque, New Mexico 87123, USA*
[3]*California NanoSystems Institute, University of California - Los Angeles, California 90095, USA*
[†]*These authors contributed equally to this work.*
arafin.1@osu.edu

This Letter reports the growth, fabrication, and characterization of molecular beam epitaxy (MBE)-grown quaternary InAlGaAs/GaAs quantum dot (QD) lasers emitting at sub-900 nm. The presence of Al in QD-based active regions acts as the origin of defects and non-radiative recombination centers. Applying optimized thermal annealing annihilates the defects in *p-i-n* diodes, thus lowering the reverse leakage current by six orders of magnitude compared to as-grown devices. A systematic improvement in the optical properties of the devices is also observed in the laser devices with increasing annealing time. At an annealing temperature of 700°C for 180 s, Fabry–Pérot lasers exhibit a lower pulsed threshold current density at infinite length of 570 A/cm². ©
2023 Optica Publishing Group

Semiconductor quantum dots are receiving augmented research interest in the last three decades due to high material gain and ultra-low linewidth enhancement factor enabled by three-dimensional (3D) carrier confinement and atom-like discrete density of states [1,2]. Growth of a homogenous quantum dot (QD) ensemble with a high areal density is a primary requirement to achieve all the distinct benefits. Continuous improvement in material growth technology of self-assembled QDs has resulted in low-threshold, high quantum efficiency lasers with high thermal stability in the popular "telecom" and "datacom" bands where $\lambda \geq 1$ µm [3,4]. However, such progress for $\lambda \leq 1$ µm is limited despite many important applications including lidar [5], biochemical sensing [6], and solid-state laser pumping [7,8].

Al-containing InAlGaAs QDs on GaAs substrates are of particular interest due to their ability to emit in a broad spectral range from 800 nm to 1.1 µm which is inaccessible by the traditional InAs/GaAs [9] or InAs/InP [10] QDs. The presence of Al in QD-based active regions, unfortunately, causes devices to deviate from their ideal conditions. An increase in threshold current and reduction in output power are associated through formation of defects originating from oxides created by the

background gas in the ultrahigh vacuum system [11]. Moreover, a large lattice mismatch between QD layers and substrates is a prerequisite to grow self-assembled QDs in the Stranski–Krastanov growth mode which eventually induces defects and non-radiative recombination centers [12,13]. So, a detailed study on this class of QDs along with the role of defects in device performance is of supreme interest.

Remarkable improvement in the optical properties of QD systems at longer wavelengths via *in situ* or *ex situ* thermal annealing has been reported [11,14]. The effect is more pronounced in the laser characteristics as both the reverse leakage current and threshold current density of the device decrease with annihilating defects. Optical characteristics of Al-containing QD lasers in the 900-nm wavelength range were also reported [15,16]. However, detailed investigation on optoelectronic characterization subject to different annealing conditions is still missing. In this work, we analyze the electro-optical characteristics of the lasers before and after annealing. The effect of annealing duration on material quality and device performance is also discussed in detail.

InAlGaAs/GaAs QD structures reported in our study were grown in a solid source molecular beam epitaxy system. Prior to implementing into devices, photoluminescence (PL) structures with QDs embedded in $Al_{0.2}Ga_{0.8}As$ barriers on GaAs substrates, schematically shown in Fig. 1(a), were first studied. Uncapped surface QDs on the top of the structure were used for inspecting the morphology. The QD composition was carefully chosen to be $In_{0.59}Al_{0.16}Ga_{0.25}As$ for obtaining emission at less than 900 nm [7]. To obtain such QDs, 4.8 ML of materials were deposited at 520°C to initiate 3D transitions using a digital alloy method where the constituent materials $Al_{0.56}InAs$ (0.15 nm), $In_{0.17}GaAs$ (0.2 nm), and InAs (0.35 nm) were deposited in 2 cycles. Ga, In, and Al growth rates were set to 0.5 ML/s, 0.1 ML/s, and 0.125 ML/s. After the growth, 100 nm of SiO_2 was deposited using plasma enhanced chemical vapor deposition. The PL sample was then broken into several pieces. Each piece underwent rapid thermal annealing (RTA) for different time durations at 700°C which was the optimized temperature reported in our earlier studies [17]. Later, SiO_2 was removed using hydrofluoric acid
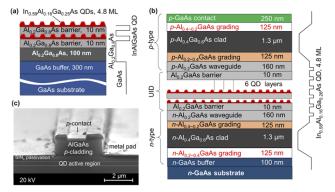
Fig. 1. 3D cross sectional schematics of the (a) PL structure and (b) laser structures with the corresponding conduction band diagrams, and (c) scanning electron microscopy (SEM) image of a fully processed Fabry–Pérot narrow-ridge laser.

Fig. 2. AFM image with dimensions of 1 μm × 1 μm and corresponding height and diameter histogram for QD PL samples. (a)–(c) For the as-grown sample and (d)–(l) for the samples annealed at 700°C for (d)–(f) 30 s, (g)–(i) 90 s, (j)–(l) 180 s.

(HF) and the sample pieces were then characterized using atomic force microscopy (AFM) and low-temperature PL spectroscopy.

The same composition of QDs was then used in the active region of laser structures along with the corresponding band diagram as shown in Fig. 1(b). To ensure high modal gain, the laser active region consisted of six QD layers embedded in 10 nm of 20% AlGaAs barriers. Prior to processing, the laser epitaxial structure was also broken into several pieces and went through the RTA process. Ridge waveguide lasers with ridge widths of 3 μm and 20 μm were fabricated through defining ridges via dry etching based on $BCl_3/Cl_2/Ar$ chemistry. Finally, the metal stacks for p- and n-contacts were evaporated, and the alloyed n-contact was annealed at 380°C. Naturally, cleaved mirror-finished facets without any high reflective (HR)/anti-reflective (AR) coatings were used for static characterization of the lasers. Figure 1(c) shows the SEM image of the fully processed device.

Figures 2(a)–2(c) contain 1 μm × 1 μm AFM images of the as-grown samples along with the histograms of QD height and diameter. For the as-grown sample, the morphological data were fitted with an asymmetric bi-Gaussian distribution, indicating the presence of two different QD families with big and small sizes. A high QD density of 5.6×10^{10} cm^{-2} was achieved for the QD ensemble required to achieve high modal gain in lasers. Upon annealing, eminent improvement in QD homogeneity was seen as the histograms are fitted with a single Gaussian curve as in Figs. 2(d)–2(l) for annealing times of 30 s, 90 s, and 180 s.

Low-temperature PL spectra for the as-grown and RTA samples are plotted in Fig. 3(a). The PL peak of the as-grown sample is seen at 767 nm which confirms sub-900 nm emission at room temperature. A broad full width at half maximum (FWHM) of 92 meV is observed, which is attributed to the inhomogeneity arising from the two QD families. Continuous increase of integrated PL intensity is seen for the QDs with increasing annealing duration up to 180 s. This is explained by the reduction in defects and the related non-radiative recombination centers [18]. Further increase of annealing time, i.e., 300 s, reduces the PL intensity which suggests the degradation of radiative recombination, but the reason is not yet understood. The process of RTA is, in general, associated with a blueshift in emission wavelength for an InGaAs/GaAs-based QD system due to interdiffusion of In-Ga atoms [19]. The same does not hold true in the InGaAlAs QDs which is probably due to the presence of Al in the QD and barrier layers. In fact, a stronger bond energy of Al-As compared to
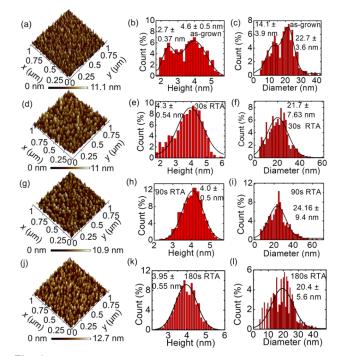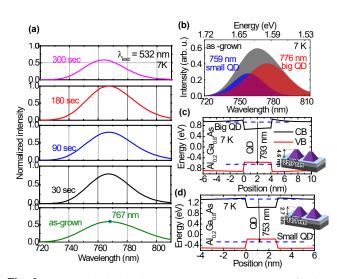

Fig. 3. Normalized photoluminescence spectra at (a) 7 K for the as-grown and annealed samples (normalized to the peak PL intensity of the sample annealed for 180 s), (b) deconvoluted PL spectrum of the as-grown sample, and (c),(d) calculated energy band diagrams for the big and small QD families.

In-As and Ga-As prevents the interdiffusion process from happening at 700°C. It should be noted that the PL FWHMs of the samples decrease with increasing annealing time. For instance, the FWHM value reduces to 76 meV for the 180-s annealed sample which results in improved size homogeneity of the QD ensemble.

The contribution of the two different QD families is further analyzed by the deconvolution of the as-grown PL spectrum into
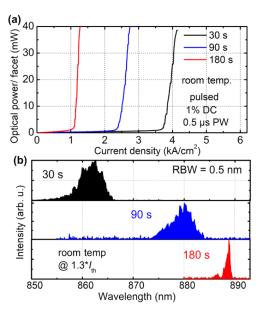
Fig. 4. (a) Pulsed *L–J* characteristics of the lasers and (b) lasing spectra of the devices annealed at different duration. DC, duty cycle; PW, pulse width; and RBW, resolution bandwidth of the optical spectrum analyzer.

Table 1. Optical Parameters of Diode Lasers Annealed at Different RTA Durations

Parameter	30-s RTA	90-s RTA	180-s RTA
Threshold current density at infinite length $J_{th,\infty}$ (KA/cm^2)	0.89	0.8	0.57
Internal loss α_i (cm^{-1})	6.7	5.7	1.3
Internal efficiency η_i (%)	88	88.6	92
Modal gain Γg_0 (cm^{-1})	4.5	3.3	3.6
Transparency current density J_{tr} (A/cm^2)	124	240	160

and barriers. This might result in a reduced band offset between the QDs and barriers, and lead to the redshift in the emission wavelength [20,21]. Further microscopy investigations, such as high-resolution transmission electron microscopy with sufficient spatial resolution, are required to fully understand the underlying mechanisms behind this phenomenon.

Electrical characterization was carried out on all four samples by measuring temperature-dependent continuous wave (CW) *J–V* characteristics as shown in Fig. 5(a). A high dark current of the order of 10^{-2} A/cm^2 is seen for the as-grown sample at -1 V at room temperature. The origin of this high dark current is attributed to a high density of crystal defects. Continuous reduction in reverse leakage current with increasing annealing durations is also evident in the RTA-processed lasers, which is consistent with the optical results. The 180-s annealed sample exhibits a very low reverse leakage current density of 10^{-12} A/cm^2. In the forward bias regime, a perfect *p-i-n* diode-like behavior of the annealed QD lasers with an ideality factor $n\sim2$ is seen in the plot, indicating radiative recombination to be the dominant current conduction mechanism. However, an *n* value ≥5 for the lasers processed using the as-grown materials suggests the presence of defect-assisted tunneling [22,23]. This is corroborated by the measured thermal activation energy E_a of the QD lasers. For the as-grown sample, a small E_a value of 70 meV at -1 V results from the weak dependence of dark current on temperature, indicating the presence of a defect-assisted tunneling current. For the samples annealed for 30 s, 90 s, and 180 s, the measured E_a values at -1 V bias are 0.2 eV, 0.58 eV, and 0.65 eV, respectively. The E_a value for the 180-s sample is comparable to half of the bandgap, suggesting that the current conduction mechanism is dominated by a bulk process such as generation-recombination (*G-R*) under reverse biasing [24].

Another interesting factor is the increment of shunt resistance R_{sh} with increasing annealing duration. Here, "R_{sh}" is represented as a parallel resistance in the equivalent circuit of a laser, which ideally has an infinite value but decreases with the decline in material quality and allows flow of current through the shunt path instead of the active region eventually deteriorating the device performance [25]. The presence of low R_{sh} is understood by the ohmic behavior of the diode's *J–V* characteristics [25]. The peak value of the differential resistance versus voltage plots in Fig. 5(b) is considered to be the value of R_{sh}. The rectification ratio is six orders of magnitude higher for the 180-s annealed devices compared to the as-grown sample, as can be understood from the *J–V* curves of the samples. Compared to the annealed devices, the symmetric *J–V* characteristics indicate the existence of a low-resistive shunt path in the as-grown sample. Note that the measured series resistances R_s of the lasers are
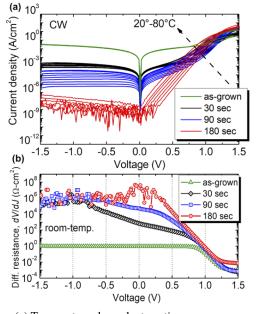
two separate spectra as shown in Fig. 3(b). The short and long wavelengths at 759 nm and 776 nm are assumed to originate from the small and big QD families, respectively. The morphological data of the big and small QD families were implemented into a 6-band *k.p.* model. The calculated transition wavelengths are 753 nm and 793 nm at 7 K as shown in Figs. 3(c) and 3(d), respectively, which is in agreement with the experimental observations. Such inhomogeneity in the QD ensembles is undesired as it causes broadening in the PL linewidth.

Due to high optical loss, no stimulated emission was achieved from the as-grown laser materials. Lasing is achieved in all the annealed samples. Figure 4(a) presents the pulsed light output versus current density (*L–J*) characteristics of the Fabry–Pérot lasers with a cavity length of 1200 µm and width 20 µm. Due to the decrease in optical loss and improvement in current injection efficiency, the threshold current density of the devices continues to lessen with increasing annealing time duration. A factor of 3.5 reduction in threshold current density is seen for the QD laser annealed from 30 s to 180 s. Laser internal parameters calculated from the *L–I* characteristics of different cavity length are listed in Table 1. A regular performance improvement with increasing annealing duration is seen for the QD samples which is consistent with the PL spectra. A reduced threshold current density at infinite length and increased injection efficiency corroborates our claims of improvement in material quality.

The stimulated emission spectra of the QD lasers are plotted in Fig. 4(b). One interesting factor is the continuous redshift of the QD laser with increasing annealing duration as the central lasing wavelength is achieved at 860 nm, 880 nm, and 890 nm for the QD laser sample annealed at 30 s, 90 s, and 180 s, respectively. The strong redshift of the lasing spectra with increasing annealing duration is not yet fully understood. Strain relaxation and interdiffusion of the InAlGaAs QDs with the AlGaAs barrier materials are some possible reasons. During annealing, high temperature can promote the interdiffusion of the material components, which may affect the electronic structure of the QDs

Fig. 5. (a) Temperature-dependent continuous wave current density versus voltage (*J–V*) characteristics of the QD lasers with different annealing duration, and (b) extracted differential resistance versus voltage characteristics.

1.2 Ω, 1.4 Ω, 1.4 Ω, and 4.6 Ω for the as-grown, 30-s-, 90-s-, and 180-s-annealed samples, respectively. The slight increase in R_s in the 180-s sample could be due to random measurement errors.

QD lasers emitting at shorter than 900 nm are important for several applications which benefit from the distinct advantages offered by QDs. A comprehensive study on the quaternary InAl-GaAs QD materials as well as the resulting devices is conducted. The impact of annealing on Al-containing QD materials is analyzed in detail. Further optimization in QD growth with *in situ* annealing as well as engineering the active region with modulation such as *p*-doping [26] or tunneling injection [27] can outperform the reported devices.

REFERENCES

1. D. Bimberg, M. Grundmann, and N. N. Ledentsov, *Quantum dot heterostructures* (John Wiley & Sons, 1999).
2. V. M. Ustinov, A. E. Zhukov, A. E. Zhokov, N. A. Maleev, and A. Y. Egorov, *Quantum Dot Lasers* (Oxford University Press on Demand, 2003).
3. J. Duan, H. Huang, B. Dong, D. Jung, J. C. Norman, J. E. Bowers, and F. Grillot, IEEE Photonics Technol. Lett. **31**, 345 (2019).
4. T. Septon, A. Becker, S. Gosh, G. Shtendel, V. Sichkovskyi, F. Schnabel, A. Sengül, M. Bjelica, B. Witzigmann, and J. P. Reithmaier, Optica **6**, 1071 (2019).
5. M. Kutila, P. Pyykönen, H. Holzhüter, M. Colomb, and P. Duthon, *International Conference on Intelligent Transportation Systems*, (IEEE, 2018), pp. 1695–1701.
6. J. P. Giraldo, M. P. Landry, S. M. Faltermeier, T. P. McNicholas, N. M. Iverson, A. A. Boghossian, N. F. Reuel, A. J. Hilmer, F. Sen, and J. A. Brew, Nat. Mater. **13**, 400 (2014).
7. S. Lee, R. Arefin, H. Jung, J. Ha, M. S. Islam Sumon, J. S. Kim, S. Krishna, and S. Arafin, J. Appl. Phys. **131**, 233104 (2022).
8. T. W. Schlereth, C. Schneider, S. Gerhard, S. Hofling, and A. Forchel, IEEE J. Sel. Top Quantum. Electron. **15**, 792 (2009).
9. R. Leon, P. Petroff, D. Leonard, and S. Fafard, Science **267**, 1966 (1995).
10. D. Gready, G. Eisenstein, V. Ivanov, C. Gilfert, F. Schnabel, A. Rippien, J. P. Reithmaier, and C. Bornholdt, IEEE Photonics Technol. Lett. **26**, 11 (2014).
11. S. Bauer, V. Sichkovskyi, F. Schnabel, A. Sengül, and J. P. Reithmaier, J. Cryst. Growth **516**, 34 (2019).
12. A. Baskaran and P. Smereka, J. Appl. Phys. **111**, 044321 (2012).
13. A. Sakai and T. Tatsumi, Phys. Rev. Lett. **71**, 4007 (1993).
14. S. Malik, C. Roberts, R. Murray, and M. Pate, Appl. Phys. Lett. **71**, 1987 (1997).
15. T. W. Schlereth, S. Gerhard, W. Kaiser, S. Hofling, and A. Forchel, IEEE Photonics Technol. Lett. **19**, 1380 (2007).
16. S. Fafard, K. Hinzer, S. Raymond, M. Dion, J. McCaffrey, Y. Feng, and S. Charbonneau, Science **274**, 1350 (1996).
17. R. Arefin, S. Lee, H. Jung, J. Ha, W. You, A. Ghosh, M. S. I. Sumon, J. S. Kim, S. Krishna, and S. Arafin, *Compound Semiconductor Week*, 1 (2022).
18. W. Jiang, H. Xu, B. Xu, X. Ye, J. Wu, D. Ding, J. Liang, and Z. Wang, J. Cryst. Growth **212**, 356 (2000).
19. T. Torchynska, A. V. Hernandez, G. Polupan, and E. V. Lozada, Mater. Sci. Eng. B **176**, 331 (2011).
20. S. Sanguinetti, T. Mano, A. Gerosa, C. Somaschini, S. Bietti, N. Koguchi, E. Grilli, M. Guzzi, M. Gurioli, and M. Abbarchi, J. Appl. Phys. **104**, 113519 (2008).
21. J. S. Kim, J. H. Lee, S. U. Hong, W. S. Han, H.-S. Kwack, J. H. Kim, and D. K. Oh, J. Appl. Phys. **94**, 2486 (2003).
22. Z. Wang, M. Zhu, X. Chen, Q. Yan, and J. Zhang, Microelectron. Eng. **103**, 36 (2013).
23. P. Perlin, M. Osiński, P. G. Eliseev, V. A. Smagley, J. Mu, M. Banas, and P. Sartori, Appl. Phys. Lett. **69**, 1680 (1996).
24. B. Marozas, W. Hughes, X. Du, D. Sidor, G. Savich, and G. Wicks, Opt. Mater. Express **8**, 1419 (2018).
25. S. Dongaonkar, Y. Karthik, D. Wang, M. Frei, S. Mahapatra, and M. A. Alam, IEEE Electron. Dev. Lett. **31**, 1499 (2010).
26. Q. Li, X. Wang, Z. Zhang, H. Chen, Y. Huang, C. Hou, J. Wang, R. Zhang, J. Ning, and J. Min, ACS Photonics **5**, 1084 (2018).
27. I. Khanonkin, S. Bauer, V. Mikhelashvili, O. Eyal, M. Lorke, F. Jahnke, J. P. Reithmaier, and G. Eisenstein, Progress Quantum Electron. **81**, 100362 (2022).